Engineering Failure Analysis 57 (2015) 219–235

Contents lists available at ScienceDirect

Engineering Failure Analysis

journal homepage: www.elsevier.com/locate/efa

Failure analysis for coming out of shaft from shrink-fitted ceramic sleeve

Nao-Aki Noda *, Dedi Suryadi, Seiichi Kumasaki, Yoshikazu Sano, Yasushi Takase

Department of Mechanical Engineering, Kyushu Institute of Technology, 1-1 Sensui-cho Tobata-ku, Kitakyushu-shi 804-8550, Japan

ARTICLE INFO

Article history:
Received 10 March 2015
Received in revised form 7 June 2015
Accepted 11 July 2015
Available online 28 July 2015

Keywords:
Coming out of shaft
Ceramic sleeve
Shrink fitting
Finite element method
Roller structure

ABSTRACT

This paper deals with failure analysis for coming out of the steel shaft from ceramic sleeve connected by shrink fitting. Only low shrink fitting ratio can be applied because of the brittleness of the ceramic sleeve. However, the steel shafts may be loosening out from the ceramic sleeve under such low shrink fitting ratio. In this study, the coming out behavior of the shaft during rotation is analyzed by the finite element method. The roller rotation is replaced by shifted load in the circumferential direction on the fixed roller. It is found that the load rotation can be approximated by the discrete load shifting at the interval angle $\theta_0 = 12^\circ$ within 1% error. The effect of the shrink fitting ratio on the coming out of the shaft is discussed as well as several other parameters, such as Young's modulus of the shaft, the friction coefficient, magnitude of the load, and geometry of the shaft. Furthermore, it is found that the shear stress distribution at the shrink-fitted area may be useful for evaluating whether the coming out occurs or not.

1. Introduction

Steel conveying rollers are used in the heating furnace as shown in Fig. 1 to produce high-quality steel plates for automobiles. Fig. 2(a) shows the conventional roller whose inside is cooled by water circulation to reduce the temperature although causing some energy loss and maintenance cost. The steel sleeve and steel shafts are usually connected by shrink fitting and bonded by welding, and the steel sleeve is coated by ceramic on the surface to improve wear resistance. However, the thermal expansion mismatch may induce surface failures such as crack, peeling, wearing resulting in short roller life [1].

Fig. 2(b) shows a new ceramics roller consisting of steel shafts at both ends and ceramic sleeve having high heat resistance, wear resistance [2], and corrosion resistance [3]. All ceramic sleeve may prevent most of the defects observed at coated ceramic, and therefore, the roller life can be extended significantly. Since adhesive bonding and metal bonding have very low strength under high temperature, only shrink fitting can be applied for ceramic sleeve and steel shaft connection used in the heating furnace [4–7]. The thermal expansion coefficient of steel is about four times larger than that of ceramic having low fracture toughness [8,9], attention should be paid to the risk of ceramic sleeve fracture.

In the previous study the authors have considered similar ceramic structures under high temperature environment in continuous galvanizing line [10,11], in the continuous pickling line [12], and in the heating furnace [13]. It should be noted that only low shrink fitting ratio can be applied for those structures because of the ceramic brittleness.

As an example, similar all ceramic rolls have been successfully developed to be used in a molten metal bath in continuous galvanized steel line [9–11]; however, coming out of the shaft was observed several times in prototype rolls. Since sliding bearings for rolls and rollers do not restrict the axial movement of the shaft, the coming out can be problematic. Even when the shaft movement is restricted within a small allowable range, the coming out of the shaft may cause local thrust loading, frictional heat generation, and wear

* Corresponding author.
E-mail address: noda@mech.kyutech.ac.jp (N.-A. Noda).

http://dx.doi.org/10.1016/j.engfailanal.2015.07.016
1350-6307/

Nomenclature

δ	diameter difference [mm]
d	inner diameter of the sleeve [mm]
T	sleeve thickness [mm]
t	shaft thickness [mm]
L	contact length [mm]
w	distributed load on the roller surface [N/mm]
ρ	mass density [kg/m^3]
ν	Poisson's ratio
μ	friction coefficient
δ/d	shrink fitting ratio
a	outer diameter of the sleeve [mm]
b	inner diameter of the sleeve [mm]
N	number of cycle
E_{sl}	Young's modulus of the ceramic sleeve [GPa]
E_{sh}	Young's modulus of the steel shaft [GPa]
θ_0	interval of load shift angle in the simulation
u_{zA}	displacement at point A [mm]
u_{zC}	displacement at center point [mm]
σ_r	radial stress on the contact part [MPa]
τ_{rz}	shear stress at z-direction [MPa]

preventing smooth rotation of the roller. Previously, Truman and Booker investigated micro-slipping between the gear hub and shaft connected by shrink fitting [14]. Antony analyzed contact separation for rotating thermos-elastoplastic shrink fit assembly [15]. However, few failure studies are available for coming out of the shaft from the shrink-fitted ceramics sleeve.

In this paper, therefore, the coming out behavior of the steel shaft from the ceramic sleeve will be considered during operation. The finite element method is applied to simulate the behavior. Then, several mechanical factors will be considered to understand the coming out of the shaft.

2. Analysis conditions

2.1. Shrink fitting connection with roller dimensions

Fig. 3 shows dimensions of the roller considered whose outer diameter D = 300 mm. Here, the roller consists of ceramic sleeve and steel shaft connected by shrink fitting. The shrink fitting ratio is defined as δ/d, where δ is the diameter difference and d is the inner

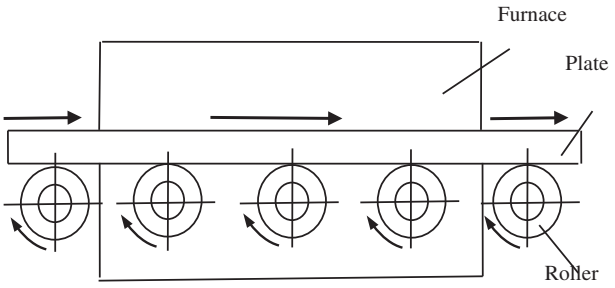

Fig. 1. Layout of rollers in heating furnace.

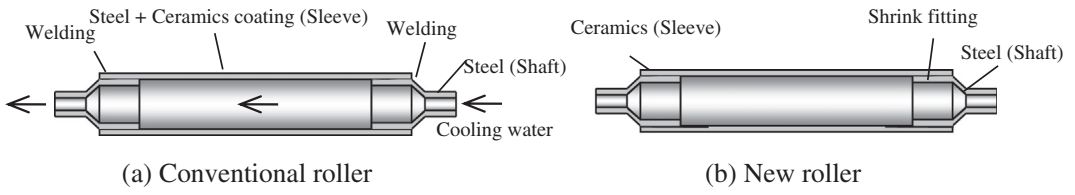

Fig. 2. Roller structure (a) Conventional roller; (b) new roller.

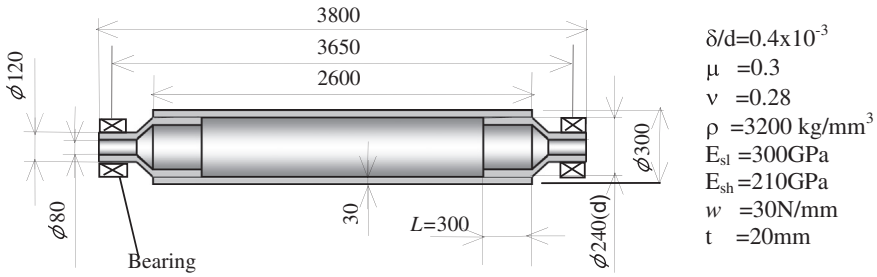

Fig. 3. Structure and dimensions of the new roller model with standard dimensions (mm).

diameter of the sleeve d = 240 mm. The shrink fitting connection was analyzed in the previous studies [4–7,12,13,16]. In Ref. [4], the ceramic roller structure was studied without considering thermal stress when a ceramic sleeve and steel solid shafts are connected by shrink fitting at both ends. The results show that for larger shrink fitting ratio $\delta/d \geq 0.2 \times 10^{-3}$, the stress due to distributed load $\sigma_{\theta b}$ becomes constant independently from δ/d. The constant value coincides with the results when the sleeve and shafts are perfectly bonded. In other words, if $\delta/d \geq 0.2 \times 10^{-3}$, the sleeve and shafts can be treated as a unit body. Moreover, in Ref. [13], the ceramic roller structure used in the heating furnace was studied focusing on thermal stress at the shrink fitting portion. The result shows that the maximum thermal stress can be reduced by using the small thickness of the steel shaft [13].

Table 1 shows mechanical properties of the materials. The shaft material is assumed as alloy steel, which is relatively inexpensive but tough enough, and the sleeve material is silicon nitride. Thermal expansion coefficients are also indicated in Table 1.

2.2. Inertial force effect due to roller rotation

In the first place, inertial force effect during the roller rotation will be considered by assuming two-dimensional rotating disk model with a circular hole as shown in Fig. 4. Here, the maximum rotating angular velocity ω = 33 rad/s can be estimated from the data for the roughing mill [17]. Although the roller data for heating furnace are not available in [17], the carrying speed is nearlythe same as the one of roughing mill. When the ceramics sleeve is rotating with the angular velocity ω, the stresses $\sigma_\theta(r)$, $\sigma_r(r)$ appearing at r = r are expressed the Eq. (1) [18].

$$\sigma_\theta(r) = \frac{3+\nu}{8}\rho\omega^2\left[b^2 + a^2 + \frac{a^2b^2}{r^2} - \frac{1+3\nu}{3+\nu}r^2\right],$$
$$\sigma_r(r) = \frac{3+\nu}{8}\rho\omega^2\left[b^2 + a^2 - \frac{a^2b^2}{r^2} - r^2\right] \quad (1)$$

where a is outer radius, b is inner radius, r is radius at the point, ν is Poisson's ratio, ρ is mass density. By substituting b = 120 mm, a = 150 mm, r = b = 120 mm, ν = 0.28, ρ = 3200 kg/mm^3 in Fig. 3 into (1), we have $\sigma_\theta(b) = 0.073$ MPa, $\sigma_r(b) = 0$ and the radius expansion $\Delta b = \varepsilon_\theta \cdot b = \sigma_\theta(b)/E_{sh} = 2.94 \times 10^{-5}$ mm.

Here we only consider the ceramic sleeve rotation without considering the shaft rotation to estimate the dynamic effect safely. Due to the inertial force effect, the inner radius of the ceramic sleeve may expand only $\Delta b = 2.94 \times 10^{-5}$ mm. Then the shrink fitting ratio may be reduced by only 0.12%. Since the inertial force can be neglected, a quasi-static analysis will be proposed in the following section.

2.3. Coming out simulation for the rotating roller

In this study, the coming out of the shaft will be realized on the numerical simulation. Here, the coming out of the shaft is considered under room temperature because the coming out occurs more easily. When we consider the roller in the heating furnace, equivalent shrink fitting ratios may be applied by considering the shaft expansion because the thermal expansion

Table 1
Properties of materials.

Properties	Ceramic	Steel
Young's modulus [GPa]	300	210
Poisson's ratio	0.28	0.3
Tensile strength [MPa]	500	600
Mass density [kg/m^3]	3200	7800
Thermal expansion coefficient [1/K]	0.3×10^{-5}	1.2×10^{-5}

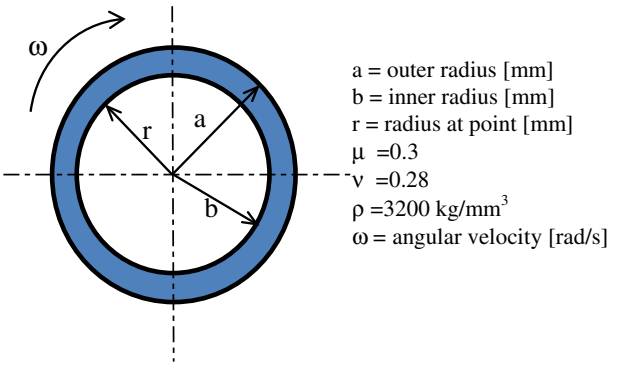

Fig. 4. Two-dimensional of rotating disk with a circular hole.

coefficient of the steel shaft is four times larger than the one of ceramic (see Table 1). Here, the shrink fitting ratio is considered in the range $\delta/d = 0.01 \times 10^{-3}$–$1.0 \times 10^{-3}$ at room temperature.

Fig. 5 shows the roller rotation under loading where Point A located at the bottom of the shaft moves to the top after rotating 180° as shown in Fig. 5(b). To simulate the coming out behavior, the roll rotation is replaced by the shifted load w in the circumferential direction on the fixed roll as shown in Fig. 6. The roller is subjected to distributed load $w = 30$ N/mm as the weight of the conveyed steel assuming the shaft ends are simply supported. As shown in Fig. 6, the continuous load shifting can be replaced by discrete load shifting with load shift angle θ_0, which is usually used as a standard discretization numerical analysis. The suitable shift angle will be considered with the numerical results in Section 3.3. In other words, the rotation of the roller under loading is replaced by the non-rotating roller subjected to load shifting in the circumferential direction. Then, to obtain the solution numerically, the continuous load shifting is replaced by discrete load shifting in the circumferential direction at the interval θ_0. Here, the initial load position $\theta_0 = 0°$ is corresponding to the number of cycle N = 0, and $\theta = 360°$ is corresponding to the number of cycle N = 1.

Fig. 7 shows the load conditions. Here, a sliding bearing is assumed for the model, which does not constrain the shaft movement. Due to the symmetry Fig. 7 show the half model considered with the total number of element 154,320. The smallest element size at the contact portion between sleeve and shaft is 1.25 mm × 1.25 mm × 6 mm. Static structural analysis is performed to the roller by using MSC Marc Mentat 2011 [19] with full Newton–Raphson iterative sparse solver of multifrontal method. In this study, a three-dimensional elastic FEM analysis can be applied because the loading condition does not exceed the yielding stress for the steel shaft, and the macroscopic plastic deformation does not appear for ceramics sleeve until failure.

The effect of the torsional load at the contact portion can be ignored because the shear stress $\tau_{r\theta}$ is very small compared to the shear stress τ_{rz} [13]. In contact analysis, it is known that two types of friction models, that is, stick–slip model and bilinear model have good accuracy [19]. However, since the stick–slip model needs large amount of data to determine friction force during repetitive calculation process, in this study the bilinear model is applied where the friction force is simply determined from the displacement. The friction coefficient between sleeve and shaft at joint portion is assumed as $\mu = 0.3$. All conditions above are used as a reference condition.

3. Evaluation for the coming out and deformation of the shaft due to the distributed load and shrink fitting

3.1. Deformation and stresses of the shaft caused by shrink fitting

In order to consider coming out behavior, the shaft deformation due to shrink fitting is investigated in the first place. Fig. 8 illustrates the shaft deformation with the (r,z) coordinate defined before shrink fitting. The displacement u_{zC} in the z-direction is

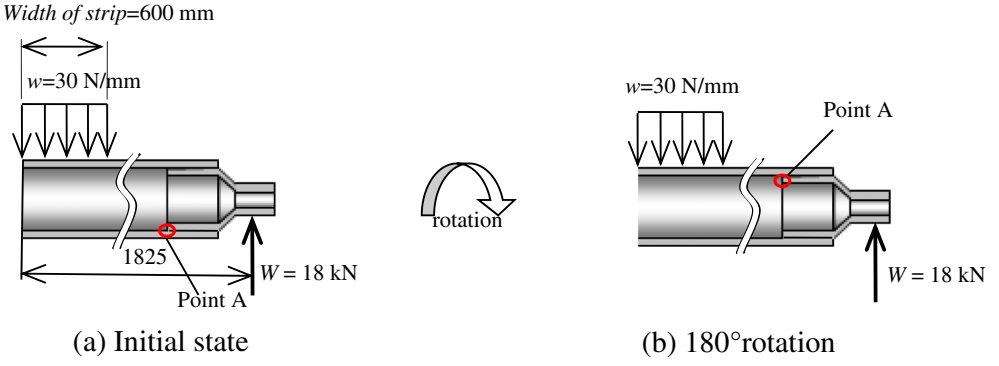

Fig. 5. Dimensions and loading condition of new roller (a) initial state; (b) 180° rotation.

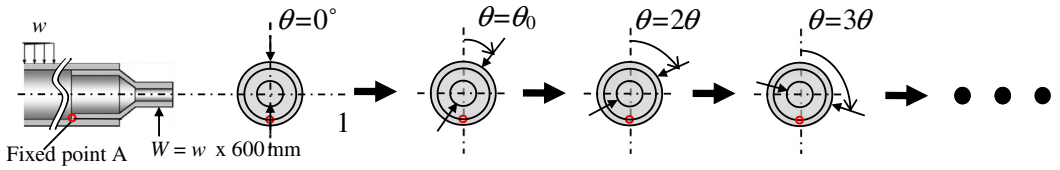

Fig. 6. The rotation of the roller replaced by the shifted load at the interval of the load shift angle θ_0. When $\theta = 0°$the number of cycle N = 0, and when $\theta = 360°$ the number of cycle N = 1.

determined from the values at 4 points as $u_{zC}^{sh} = (u_{zA}^{sh} + u_{zA}^{sh}{}' + u_{zB}^{sh} + u_{zB}^{sh}{}') / 4 = u_{zA}^{sh} < 0$ as shown in Fig. 8(a). Then, since the shaft is under compression in the r-direction; we have $u_{zA}^{sh} = u_{zC}^{sh} < 0$.

Fig. 8(b) shows stress σ_r distribution appearing along the contact surface due to shrink fitting with the maximum compressive stress $\sigma_r = 120$ MPa. Fig. 8(c) shows shear stress τ_{rz} distribution due to shrink fitting with the maximum stress $\tau_{rz} = 30$ MPa. The shaft is extended in the z-direction by the compressive stress σ_r due to shrink fitting, but the shear stress τ_{rz} may prevent the elongation. Since the shaft end surface tends to be significantly deformed by the compressive stress, the maximum shear stress may be important.

3.2. Displacement and deformation of the shaft due to the initial load

Fig. 9(a) shows the shaft after several number of loading cycle N, which defines the displacement u_{zA} at point A and u_{zC} at point C in the (r,z) coordinate. Fig. 9(b) shows the shaft due to initial distributed load N = 0 focusing on the displacement $u_{zA}^{N=0}$. As shown in Fig. 9(b), the positive displacement $u_{zA}^{N=0} (> 0 > u_{zA}^{sh})$appears at point A although the displacement due to shrink fitting was negative$u_{zA}^{sh} < 0$ as shown in Fig. 8(a). On the other hand, at point C, the displacement $u_{zC}^{N=0} (> u_{zC}^{sh})$ appears but usually still negative $u_{zC}^{N=0} < 0$. Those values $u_{zA}^{N=0}$ and $u_{zC}^{N=0}$ are defined as the initial displacement at N = 0 considering both shrink fitting and initial loading.

Figs. 10 and 11 show the results of u_{zA} for extremely small $\delta/d = 0.01 \times 10^{-3}$ and for standard $\delta/d = 0.2 \times 10^{-3}$. Here, the friction coefficient $\mu = 0.3$ during N = 0 to N = 3 and the load shift angle $\theta_0 = 30°$ is applied. In Fig. 10, Point a′ refers to the displacement of shaft due to shrink fitting, while point a represents the initial displacement of the shaft at N = 0. Under the small shrink fitting ratio in Fig. 10, the average value of the u_{zA} at each cycle increases with increasing N. Under the standard shrink fitting ratio in Fig. 11, the average value of the u_{zA} at each cycle is almost constant although the amplitude of u_{zA} increases slightly with increasing N.

Next, the positions of peak and valley of u_{zA} are considered. Fig. 10 shows the angle of rotation at point (a), (b), (c), and (d). It is seen that the peak occurs at each number of cycle $N \cong n + 1/6$ (n = 0,1,2,..) corresponding to the rotation angle $\theta \cong 2\pi n + \pi/3$, while the valley occurs at each number of cycle $N \cong n + 2/3$ (n = 0,1,2,..) corresponding to the rotation angle $\theta \cong 2\pi n + 4\pi/3$. In other words, the peak and valley do not occur at $\theta = 0°$ and $\theta = 180°$. This is because the relative displacement between the sleeve and shaft cannot follow the load direction change immediately due to the irreversible effect of friction force.

Fig. 10 shows displacement u_{zA} of the shaft under low shrink fitting ratio $\delta/d = 0.01 \times 10^{-3}$. It is seen that the average displacement u_{zA} increases in the z-direction with increasing the cycle N, that is, the shaft moves in the coming out direction. Under large shrink fitting ratio $\delta/d = 0.2 \times 10^{-3}$ in Fig. 11, although the amplitude of displacement u_{zA} slightly increases with increasing N, the coming out is not seen.

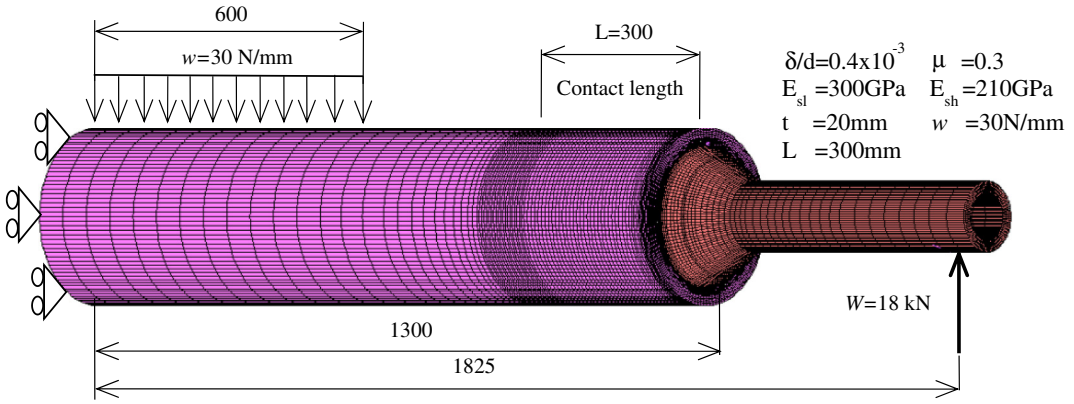

Fig. 7. Standard half model with FEM mesh.

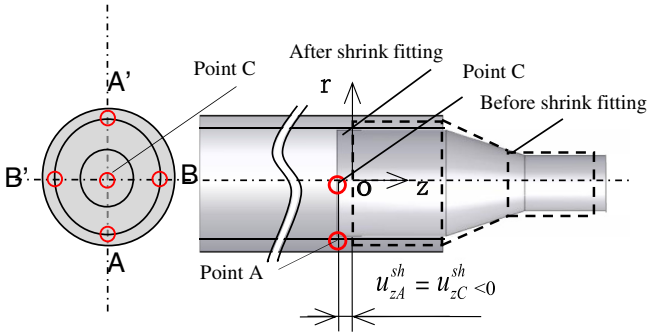

(a) Displacement due to shrink fitting $u_{zC}^{sh} = (u_{zA}^{sh} + u_{zA'}^{sh} + u_{zB}^{sh} + u_{zB'}^{sh})/4$

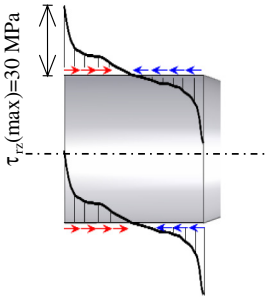

(c) Stress τ_{rz} due to shrink fitting

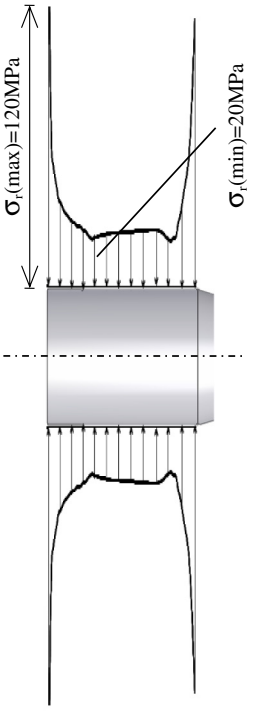

(b) Stress σ_r due to shrink fitting

Fig. 8. The z-displacement and stress of the shaft due to shrink fitting (a) the z-displacement due to shrink fitting $u_{zC}^{sh} = (u_{zA}^{sh} + u_{zA'}^{sh} + u_{zB}^{sh} + u_{zB'}^{sh})/4 = u_{zA}^{sh} < 0$; (b) stress σ_r due to shrink fitting; (c) stress τ_{rz} due to shrink fitting.

Next, the displacement at point C is considered since at the central point C the cyclic change does not appear. Fig. 12 shows the displacement u_{zC} at point C, which increases slightly at the beginning and increases significantly later under $\delta/d = 0.01 \times 10^{-3}$. On the other hand, the displacement u_{zC} increases slightly at first and becomes constant under $\delta/d = 0.2 \times 10^{-3}$. The possibility of the coming out of the shaft looks small in this case.

3.3. Load shifting angle θ_0 selection

In this study, the roller rotation under bending load is replaced by the non-rotating roller subjected to the load shifting in the circumferential direction. As a standard method of discretization in numerical analysis, the continuous load shifting can be expressed by

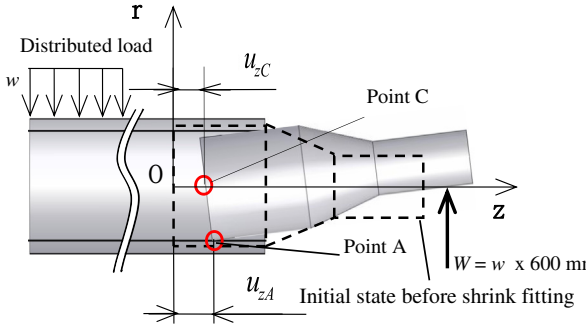

(a) Definition of z-displacement u_{zA}, u_{zC} after several number of cycle N

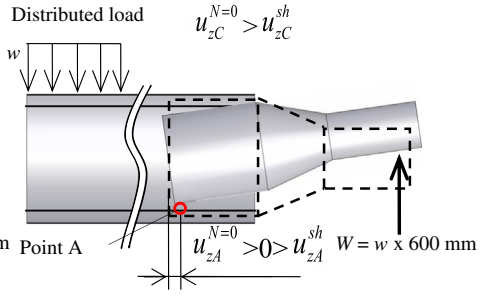

(b) The z-displacement due to shrink fitting and initial load

Fig. 9. The z-displacement of the shaft due to bending load. (a) Definition of z-displacement u_{zA}, u_{zC} after several number of cycle N; (b) the z-displacement due to shrink fitting and initial load.

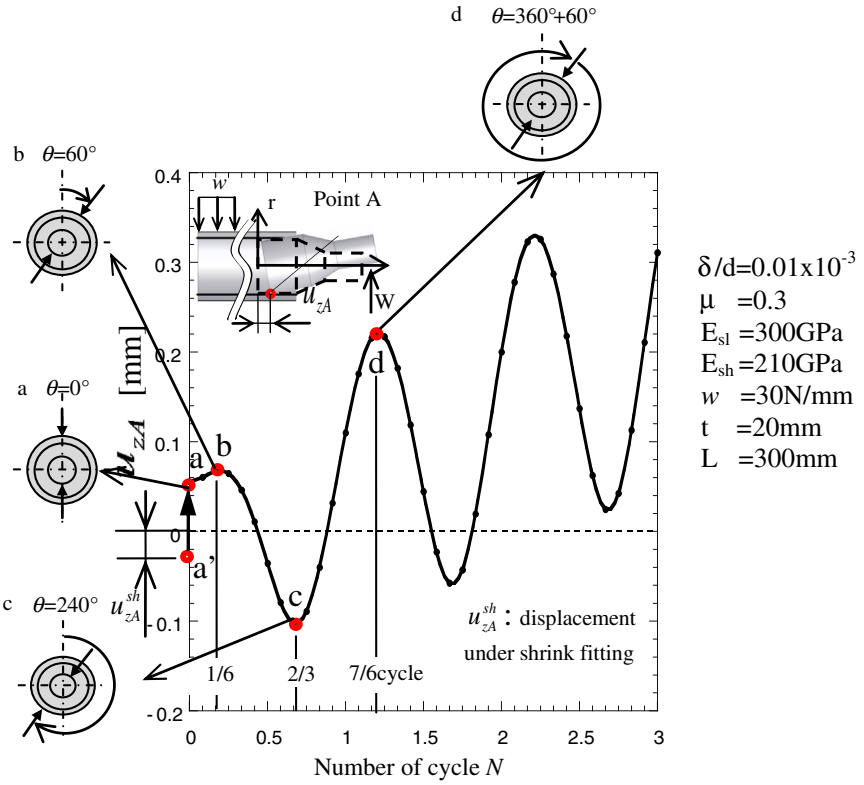

Fig. 10. The z-displacement at point A u_{zA}^{I0}vs. number of cycle N for $\delta/d = 0.01 \times 10^{-3}$ and $\mu = 0.3$ when $\theta_0 = 30°$.

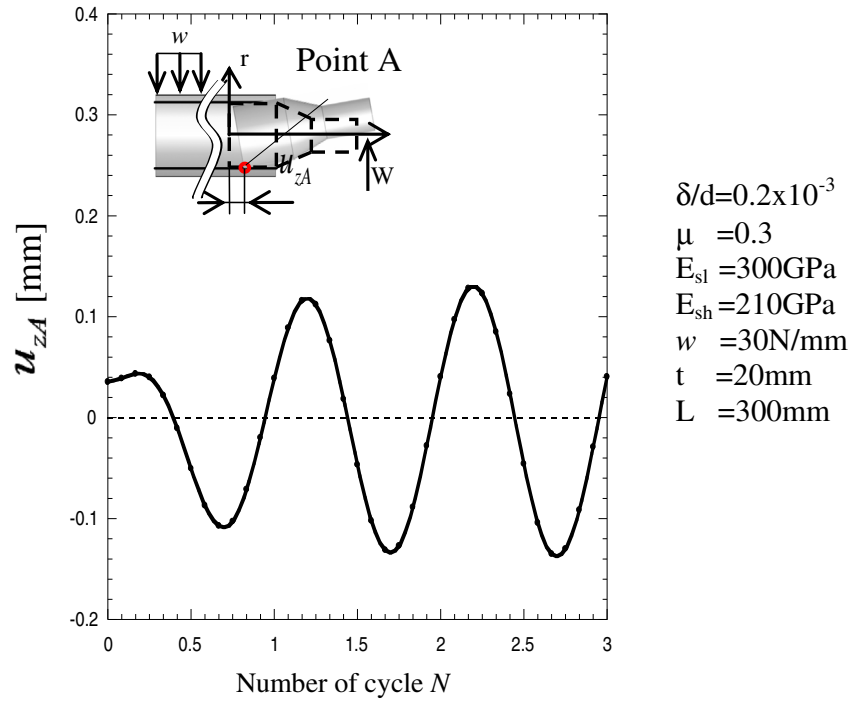

Fig. 11. The z-displacement at point A u_{zA}vs. number of cycle N for $\delta/d = 0.2 \times 10^{-3}$ and $\mu = 0.3$when $\theta_0 = 30°$.

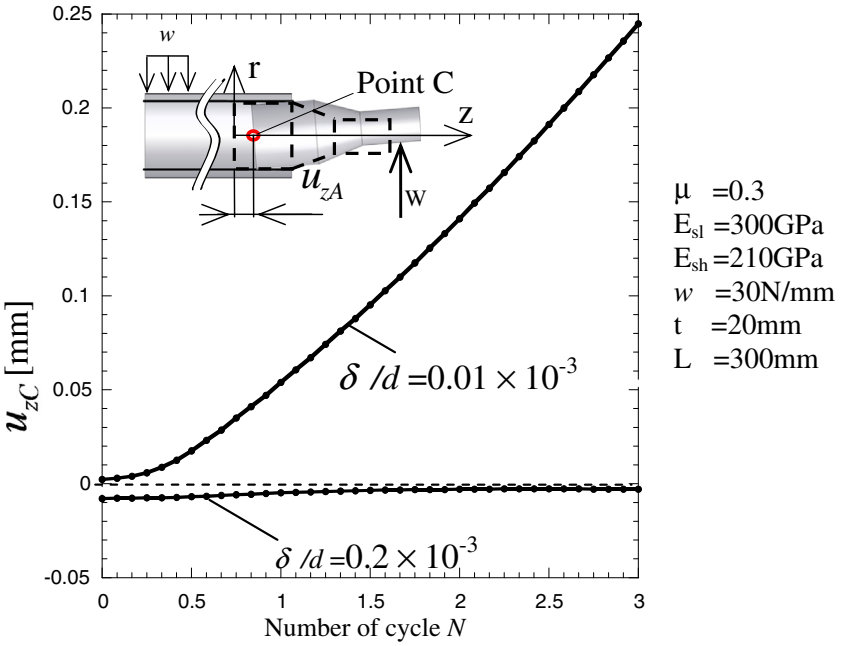

Fig. 12. The displacement point C u_{zC} vs. number of cycle N for different shrink fitting ratio when $\theta_0 = 30°$.

discrete loads at a certain interval θ_0. Here, a smaller angle θ_0 provides accurate results but large computational time. Therefore, the optimal angle θ_0 should be discussed by investigating u_{zC} with varying the shift angle, $\theta_0 = 30°$, $\theta_0 = 18°$, $\theta_0 = 12°$, and $\theta_0 = 6°$.

Fig. 13 shows u_{zA} under $\delta/d = 0.2 \times 10^{-3}$ with varying θ_0. Fig. 13 shows that smaller θ_0 provides the results for smaller amplitude of u_{zA}. However, the results converge if the $\theta_0 \leq 12°$. The discrete load shift angle $\theta_0 = 12°$ provides 30 data in one cycle, which is

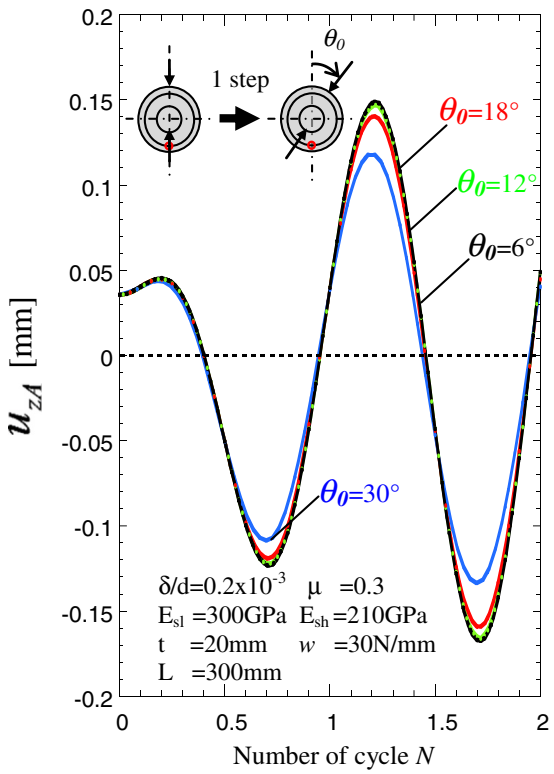

Fig. 13. The z-displacement at point A u_{zA}vs. number of cycle N for different θ_0 at $\delta/d = 0.2 \times 10^{-3}$ and $\mu = 0.3$.

enough number to present continuous displacement as shown in Fig. 13. Fig. 14 shows u_{zC} focusing on the coming out behavior. Although the result for $\theta_0 = 30°$ is very different from others, the results for $\theta_0 = 6°$ and $\theta_0 = 12°$ almost coincide with each other. Since the effect of discrete load shifting is less than 1% if $\theta_0 \le 12°$, it may be concluded that the load shifting angle $\theta_0 = 12°$ is the most suitable to reduce large calculation time without losing accuracy. In the following calculation the load shift angle $\theta_0 = 12°$ will be used consistently.

4. Effect of mechanical properties on the coming out

In this chapter, effects of several fundamental parameters, such as the shrink fitting ratio, magnitude of the load, Young's modulus, and friction coefficient are considered for the standard model whose geometry of the roller is fixed. Here, the standard model has the following:

the shrink fitting ratio $\delta/d = 0.4 \times 10^{-3}$,
the contact length L = 300 mm,
the friction coefficient between sleeve and shaft $\mu = 0.3$,
the sleeve thicknesses $T = 30$ mm,
the shaft thickness t = 20 mm,
the distributed load on the roller surface is about $w = 30$ N/mm,
Young's modulus of the ceramic sleeve $E_{sl} = 300$ GPa,
Young's modulus of steel shaft $E_{sh} = 210$ GPa.

4.1. Effect of shrink fitting ratio

In this paper, the shrink fitting ratios are considered in the range $\delta/d = 0.01 \times 10^{-3}$–$1.0 \times 10^{-3}$. Here, $\delta/d = 0.01 \times 10^{-3}$ is an example of low shrink fitting ratio. Next, $\delta/d = 0.1 \times 10^{-3}$, 0.2×10^{-3},0.4×10^{-3} may be used for real ceramics roller. Finally, $\delta/d = 1.0 \times 10^{-3}$ is an example of a larger shrink fitting ratio used for steel rollers.

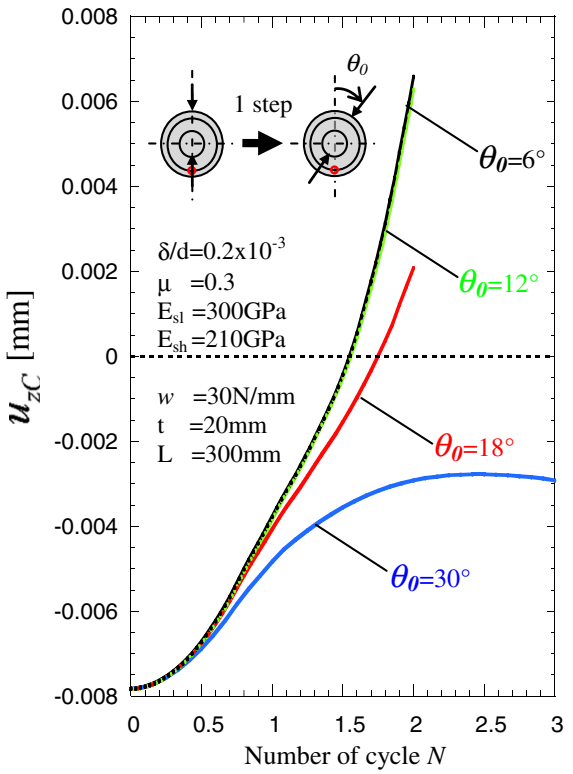

Fig. 14. The z-displacement at center point C u_{zC} vs. number of cycle N for different θ_0 when $\delta/d = 0.2 \times 10^{-3}$ and $\mu = 0.3$.

Fig. 15(a) shows the results for u_{zC}. With increasing the shrink fitting ratio, the compressive stress increases causing the negative initial value of u_{zC} as shown in Fig. 15(a) at N = 0. Under low shrink fitting ratio, the displacement u_{zC} increases significantly with increasing N.

The coming out speed is shown in Fig. 15(b). To clarify the coming out behavior, the speed of the coming out is defined as $(u_{zC}|_N - u_{zC}|_{N-0.5}) / 0.5$. Under $\delta/d = 0.01 \times 10^{-3}$–$0.1 \times 10^{-3}$, the speed increases with increasing N at N = 0–5. Under $\delta/d = 0.2 \times 10^{-3}$ the coming out speed is small, then increases after N = 4. Under $\delta/d = 0.4 \times 10^{-3}$ although the speed increases slightly at the beginning, but after N = 3 the speed becomes almost zero. Under $\delta/d = 1.0 \times 10^{-3}$ the displacement u_{zC} is always negative and the speed is always zero independent of N. In the following analysis $\delta/d = 0.4 \times 10^{-3}$ is considered as a reference condition.

4.2. Effect of the magnitude of the load

The distributed load $w = 30$ N/mm is applied to the sleeve from conveyed steel as shown in Fig. 7. In Fig. 16 the effects of the magnitude of load is investigated for $w = 15, 45, 60$ N/mm. The coming out speed significantly increases with increasing the magnitude of the load. It is seen that the coming out accelerates at N = 0–4. In other words, the coming out easily occurs when the distributed load $w \geq 45$ N/mm.

4.3. Effect of Young's modulus of the shaft

Fig. 17 shows the effect of Young's modulus of the shaft. Three types of Young's modulus are considered, namely $E_{sh} = 210$ GPa corresponding to steel, $E_{sh} = 300$ GPa corresponding to the silicon nitride ceramic, and $E_{sh} = 100$ GPa corresponding to flake graphite cast iron. The smaller Young's modulus causes larger displacement u_{zC} as well as the larger initial value in the negative at N = 0 as shown in Fig. 17 because of the larger deformation of the shaft. It is seen that when Young's modulus of shaft $E_{sh} \leq 100$ GPa the u_{zC} increases significantly with increasing number of cycle N.

4.4. Effect of the friction coefficient

Fig. 18(a) shows the effect of the coefficient of friction between the ceramic sleeve and steel shaft. The displacement u_{zC} increases with increasing N especially under smaller value of μ. However, when μ = 0.1, the behavior of u_{zc} is quite different from others because

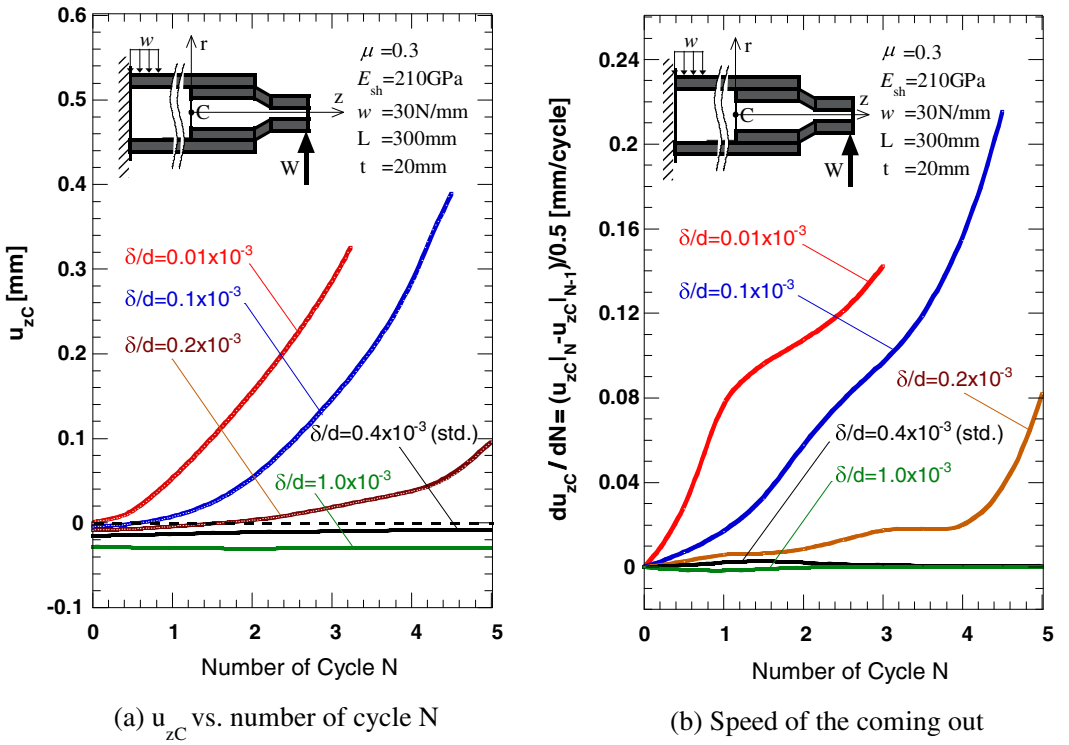

Fig. 15. Effect of the shrink fitting ratio on the coming out of the shaft (a) u_{zC} vs. number of cycle N; (b) speed of the coming out.

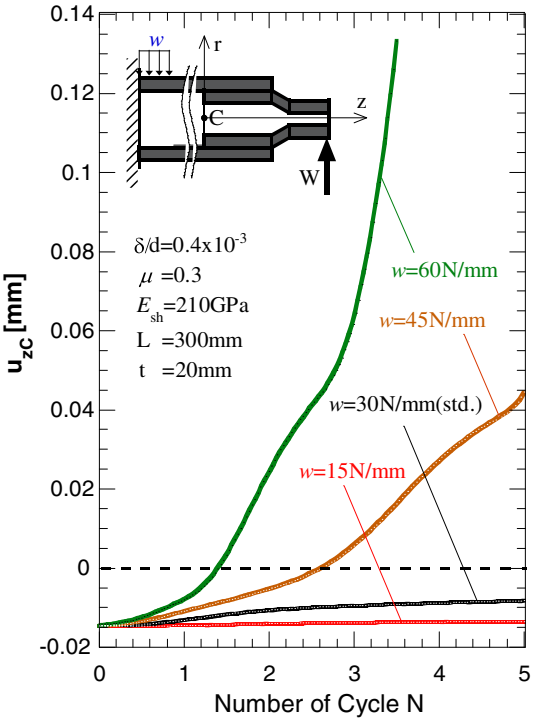

Fig. 16. Effect of distributed load when $\delta/d = 0.4 \times 10^{-3}$.

the u_{zc} has a peak at N = 1.5 and increases again at N = 2.5 and finally increases rapidly after N = 3. Fig. 18(b) shows the coming out speed clearly although most of the speed is nearly zero except for the result of μ = 0.1 after N = 3. Fig. 18 indicates that when μ ≤ 0.1 the coming out happens very easily.

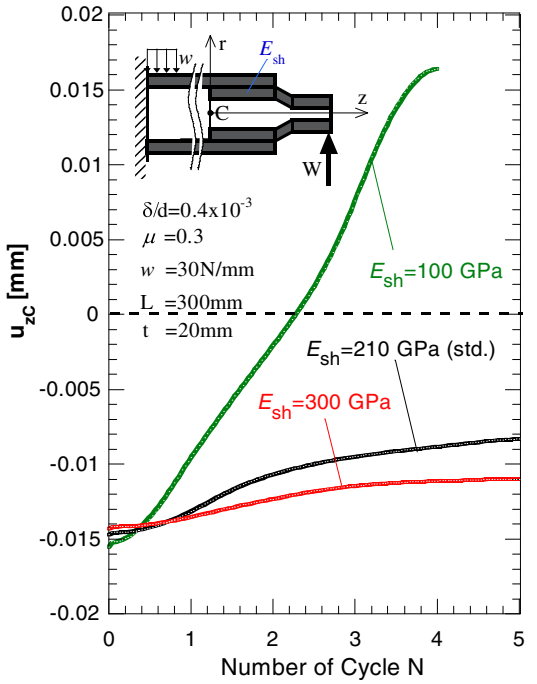

Fig. 17. Effect of Young's modulus of the shaft when $\delta/d = 0.4 \times 10^{-3}$.

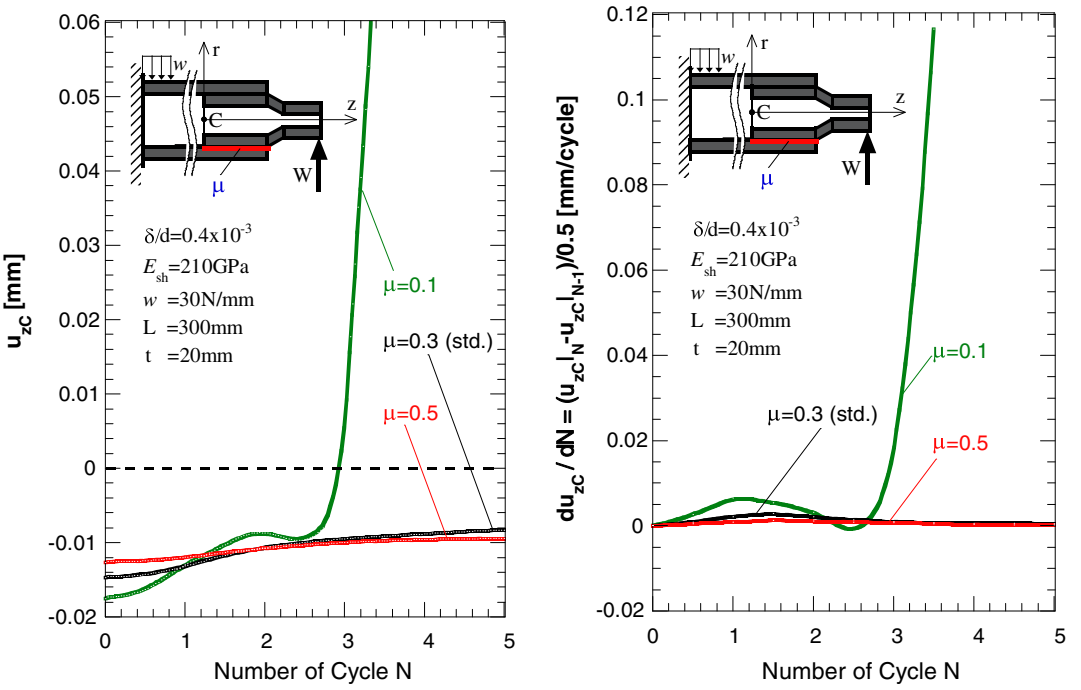

(a) u_{zC} vs. number of cycle N (b) Speed of the coming out

Fig. 18. Effect of the friction coefficient when $\delta/d = 0.4 \times 10^{-3}$ (a) u_{zC} vs. Number of cycle N; (b) speed of the coming out.

5. Effect of shaft geometry on the coming out

5.1. Effect of the shaft thickness

In the real ceramic rollers, the shaft should be designed so as to prevent the coming out. The effect of shaft geometry is considered in this chapter. Similar to the previous discussion of the shaft Young modulus, the rigidity of the shaft can be also considered by varying the shaft thickness t. Fig. 19(a),(b) show the results for different shaft thickness t = 10 mm, t = 20 mm, t = 40 mm under $\delta/d = 0.4 \times 10^{-3}$. It is seen that u_{zC} becomes larger for smaller thickness t. The difference between the results for t = 10 mm and t = 20 mm is much larger than the one for t = 20 mm and 40 mm. For t = 10 mm, the coming out speed tends to increase during N = 0–4 but becomes stable at about 0.02 mm/cycle after N = 4. Therefore Fig. 19(b) suggests that steady coming out may appear if the number of cycle N is large enough. Since the coming out speeds for t = 20 and t = 40 mm are very small, the rigidity may be enough to prevent the coming out. From Fig. 19(a) and (b), it may be concluded that when t ≤ 10 mm the coming out occurs.

5.2. Effect of the contact length of the shaft

The standard model has contact length L = 300 mm. To investigate the effect of L on u_{zC}, Fig. 20(a) shows the results for L = 120 mm, L = 150 mm, L = 240 mm, L = 480 mm. Fig. 20(a) shows when L is smaller, the displacement u_{zC} becomes larger. This is due to the larger contact length L having larger friction force.

Fig. 20(b) shows the speed of the coming out. To clarify the coming out behavior, the speed of the coming out of the shaft is defined as $(u_{zC}|_N - u_{zC}|_{N-0.5}) / 0.5$. The speed of the coming out becomes steady if N is large enough except for L = 150. For L = 450 mm, the speed is zero from N = 0. And for L = 300 mm, the steady speed appears after N = 3. The results for L = 480 mm and L = 300 mm indicate that the coming out is hard to occur. On the other hand, the speed increases with increasing number of cycle for L = 225 mm and L = 150 mm after N = 4, which means the coming out occurs easily.

6. The coming out mechanism

The coming out of the shaft has been realized in the numerical simulation as shown in previous chapters. The results are different depending on the shrink fitting ratio and other parameters. Since it is difficult to obtain the results for large number N because of large

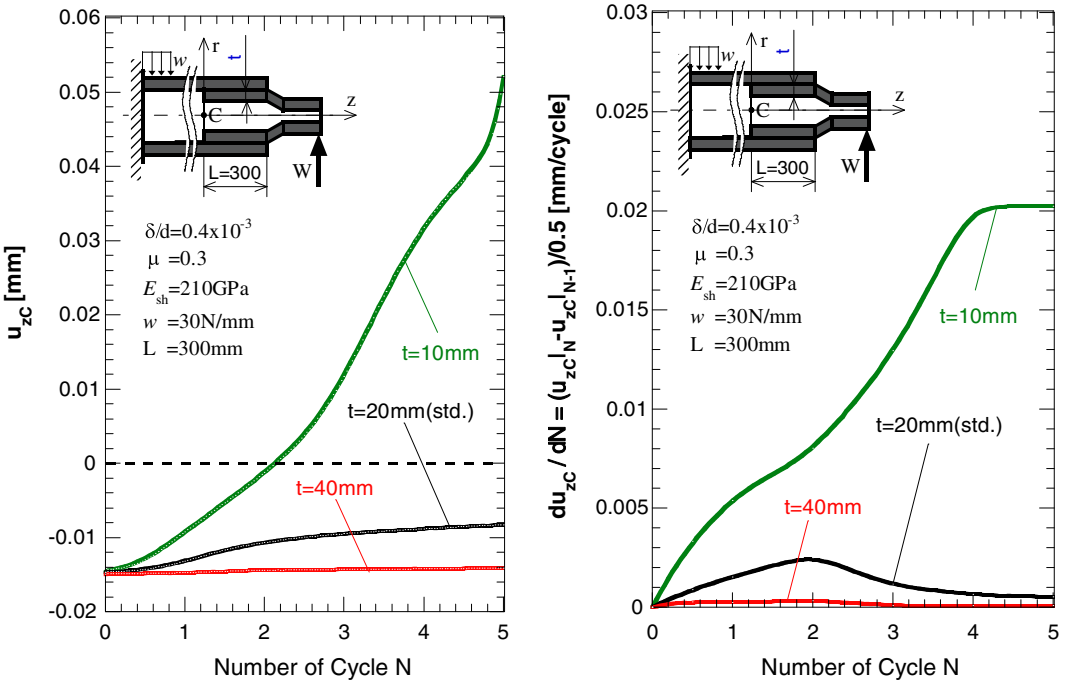

(a) u_{zC} vs. number of cycle N (b) Speed of the coming out

Fig. 19. Effect of the contacted shaft thickness when $\delta/d = 0.4 \times 10^{-3}$ and $\mu = 0.3$ (a) u_{zC} vs. number of cycle N; (b) speed of the coming out.

calculation time, it is desirable that we can judge the coming out appears or not even when N is small. In this chapter, the coming out mechanism is considered by focusing on the stress distribution appearing at the contact portion.

6.1. Investigation of shear stress τ_{rz} at contact portion due to small friction coefficient

Effects of the mechanical properties and shaft geometry on the coming out have been investigated in chapter 4 and 5. However, the unique result appears for small friction coefficient effect as shown in Fig. 18. Here, the result for $\mu = 0.1$ shows that the behavior of u_{zc} is quite different from others. This phenomenon is interesting to be investigated.

To understand the result for $\mu = 0.1$ in Fig. 18, shear stress τ_{rz} is investigated along the contact surface. Fig. 21 shows the shear stress distribution at the lower portion $\tau_{rz}(z)|_{\theta = 180^\circ}$ for different N. Note that the value of $\tau_{rz}(0)|_{\theta = 180^\circ}$ increases with decreasing the FEM mesh size, but if $z \geq 4$ mm the value of $\tau_{rz}(z)|_{\theta = 180^\circ}$ becomes mesh-independent. Fig. 22 shows the value of $\tau_{rz}(z = 5\ \text{mm})|_{\theta = 180^\circ}$ for friction coefficient $\mu = 0.1, 0.3, 0.5$. Differently from the results for $\mu = 0.3, 0.5$, the shear stress for $\mu = 0.1$ becomes zero after $N = 3$. It should be noted that the average value of shear stress $\tau_{rz}(z)|_{\theta = 180^\circ}$ is nearly zero after $N = 3$. Since the average value is nearly zero, the coming out of the shaft occurs easily without resisting the friction force due to small μ.

6.2. The coming out judgment based on shear stress distribution along contact surface

Fig. 23 shows shear the stress distribution τ_{rz} along the shaft half surface for $\theta = 0^\circ$–180° when $N = 3$. Fig. 23(a) shows the shear stress distribution under low shrink fitting ratio $\delta/d = 0.01 \times 10^{-3}$ where the coming out is likely to occur, and Fig. 23(b) shows the result under large shrink fitting ratio $\delta/d = 1.0 \times 10^{-3}$ used for steel components. Fig. 23 shows the stress distributions are very different each other. For example, in Fig. 23(a), the stress τ_{rz} changes in the circumferential direction quite largely. On the other hand in Fig. 23(b), the stress τ_{rz} does not change in the circumferential direction. The stress variation in Fig. 23(a) is due to the effect of the bending load. Fig. 23(b) is depending on the large shrink fitting stress with small effect of bending load.

Fig. 24(a) focuses on the stresses along the lines $\theta = 0^\circ$ and 180°. Here, $\tau_{rz}|_{\theta=0^\circ}$ and $\tau_{rz}|_{\theta=180^\circ}$ are compared between $N = 0$ and 3 under $\delta/d = 0.01 \times 10^{-3}$. The shear stress due to shrink fitting is approximately equal to zero except at both ends when $N = 0$. Therefore, when $N = 3$, the shear stress at shrink fitting is greatly changed, and the shear stress directions are reversed at both shaft ends. The shear stress at the left end tries to prevent the coming out of the shaft.

In Fig. 24(b), $\tau_{rz}|_{\theta=0^\circ}$ and $\tau_{rz}|_{\theta=180^\circ}$ are compared between $N = 0$ and $N = 3$ under $\delta/d = 1.0 \times 10^{-3}$. When $N = 0$, it is seen the maximum value $\tau_{rz}|_{\max} = 30$ MPa is about 600 times larger than the maximum value $\tau_{rz}|_{\max} = 0.05$ MPa in Fig. 24(a). Although

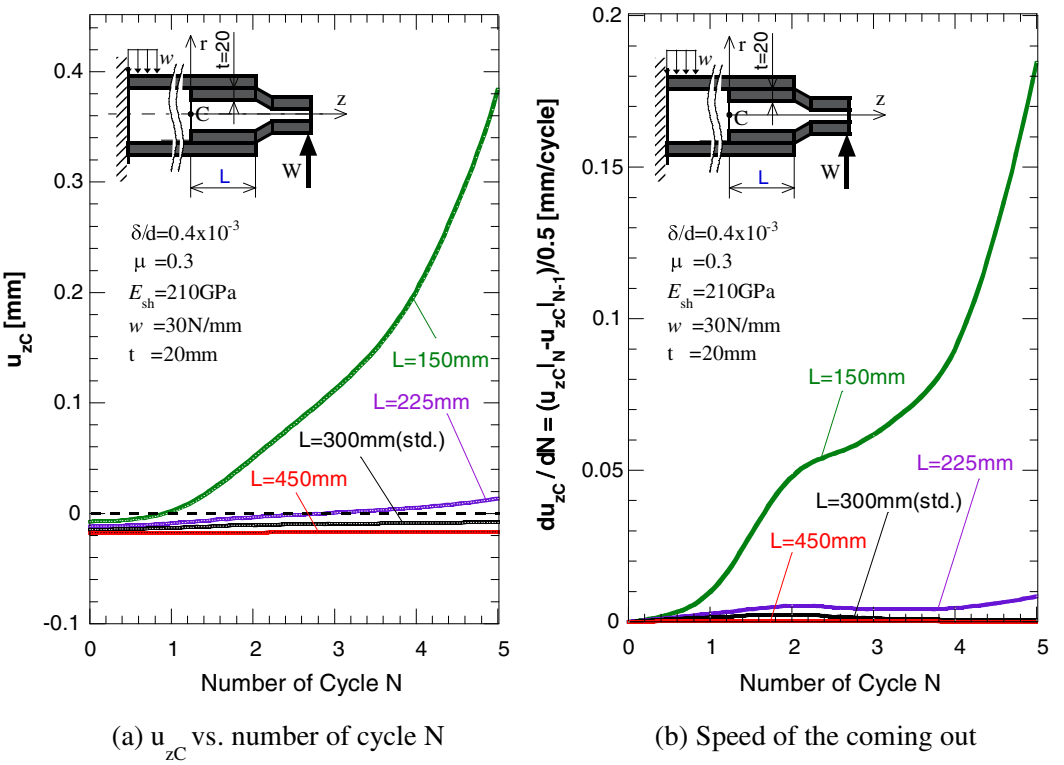

Fig. 20. Effect of the contact length when $\delta/d = 0.4 \times 10^{-3}$ and $\mu = 0.3$ (a) u_{zC} vs. number of cycle N; (b) speed of the coming out.

not indicated, the maximum compressive stress in Fig. 24(b) is about 180 times larger than the maximum compressive stress in Fig. 24(a). Due to those large shrink fitted stresses, as shown in Fig. 24(b), the effect of the bending load becomes smaller and stress does not change very much between N = 0 and N = 3 under $\delta/d = 1.0 \times 10^{-3}$.

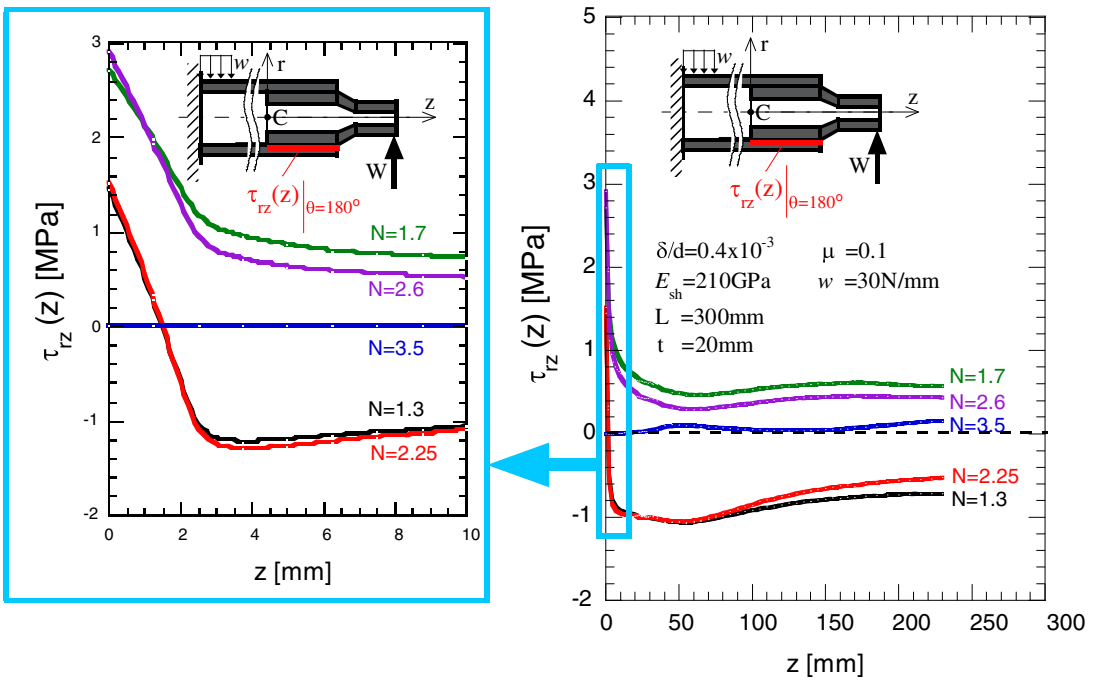

Fig. 21. Shear stress distribution along contact potion with variation of the number of cycle N when $\delta/d = 0.4 \times 10^{-3}$.

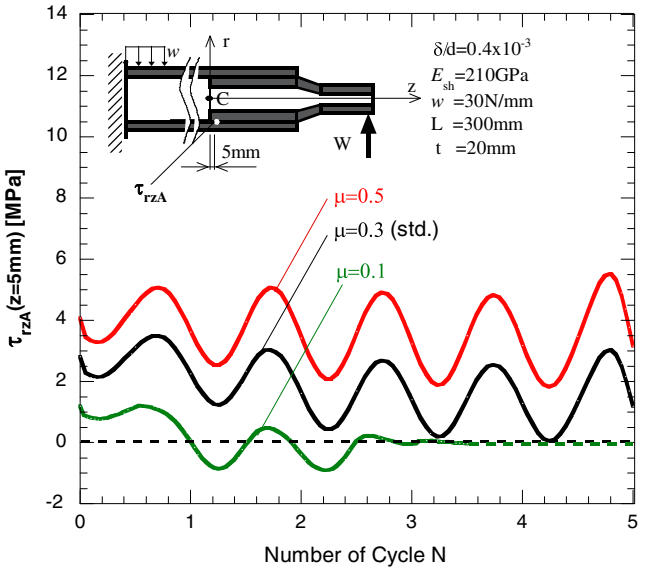

Fig. 22. Shear stress τ_{rzA} vs. number of cycle N when $\delta/d = 0.4 \times 10^{-3}$.

7. Conclusions

This paper dealt with failure analysis for coming out of the steel shaft from ceramic sleeve connected by shrink fitting. Here, inner diameter of the sleeve d = 240 mm is considered. Only low shrink fitting ratio can be applied because of the brittleness of the ceramic sleeve. In this study, the coming out behavior of the roller during rotation was analyzed by the finite element method. The conclusions can be summarized as follows:

1. In the numerical analysis the rotation of the roller under loading is replaced by the non-rotating roller subjected to shifting load in the circumferential direction. As a standard method of discretization in numerical analysis, the continuous load shifting can be replaced by discrete load shifting with less than 1% error if the load shifting interval angle $\theta_0 \le 12°$.
2. It is confirmed that the inertial force can be neglected and the quasi-static analysis presented in this paper is accurate enough.
3. The coming out of the shaft can be realized by numerical simulation. The coming out of the shaft appears under smaller shrink fitting ratio $\delta/d \le 0.2 \times 10^{-3}$ and does not appear under larger shrink fitting ratio $\delta/d \ge 0.4 \times 10^{-3}$ as shown in Fig. 15.
4. The coming out happens easily for smaller Young's modulus of the shaft $E_{sh} \le 100$ GPa, smaller friction coefficient $\mu \le 0.1$, and larger distributed load $w \ge 45$ N/mm.

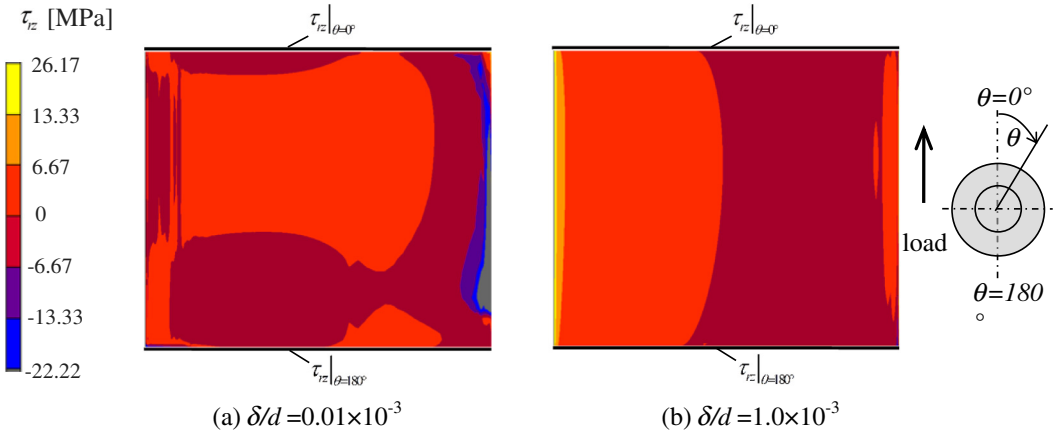

Fig. 23. Shear stress distribution τ_{rz} from $\theta = 0°$ to $\theta = 180°$ at N = 3 for (a) $\delta/d = 0.01 \times 10^{-3}$ and (b) $\delta/d = 1.0 \times 10^{-3}$.

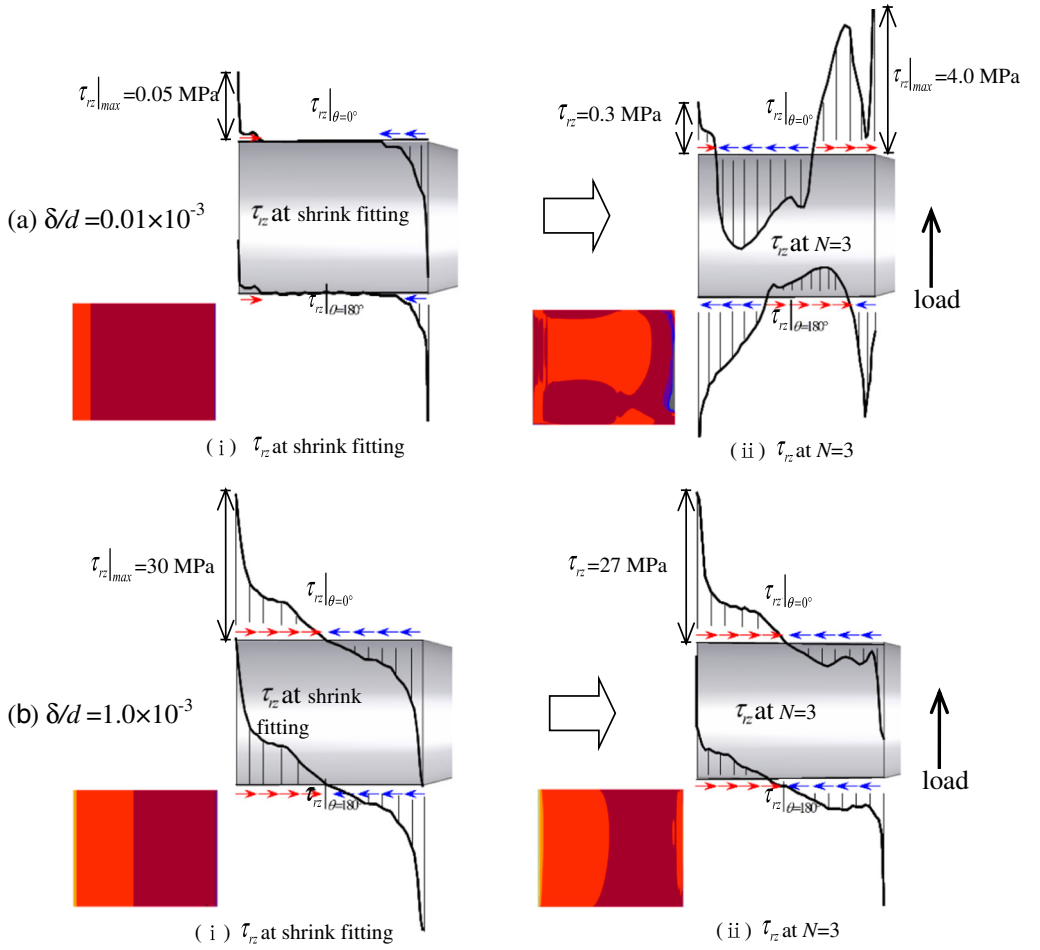

Fig. 24. Shear stress distribution τ_{rz} from $\theta = 0°$ to $\theta = 180°$ at shrink fitting and N = 3 for (a) $\delta/d = 0.01 \times 10^{-3}$ and (b) $\delta/d = 1.0 \times 10^{-3}$.

5. The speed of coming out can be prevented by increasing thickness of the shaft t ≥ 20 mm in Fig. 21 and contact length L ≥ 300 mm as shown in Fig. 22.
6. The shear contact stress is changed largely between N = 0 and N = 3 if the coming out happens, and does not change very much if no coming out. The shear contact stress change may be useful information to judge the coming out appears or not.

References

[1] M. Fujii, A. Yoshida, J. Ishimaru, S. Shigemura, K. Tani, Influence of sprayed layer thickness on rolling contact fatigue of ceramics sprayed roller, Trans. JSME Ser. C 72 (716) (2006) 1354–1360 (in Japanese).
[2] T. Ono, Current status and future prospect of the development of high performance ceramics, J. Jpn. Soc. Mech. Eng. 86 (774) (1983) 470–475 (in Japanese).
[3] C.R. Liou, T. Mori, H. Kobayashi, T. Mitamura, Influence of various atmosphere on the corrosion resistance of Si_3N_4 sintered bodies against steel making slag and its main components, J. Ceram. Soc. Jpn. 98 (4) (1990) 348–354.
[4] N.A. Noda, Hendra, Y. Takase, M. Tsuyunaru, Maximum stress for shrink fitting system used for ceramics conveying rollers, J. Solid Mech. Mater. Eng. 2 (8) (2008) 1410–1419.
[5] W. Li, N.A. Noda, H. Sakai, Y. Takase, Analysis of separation conditions for shrink fitting system used for ceramics conveying rollers, J. Solid Mech. Mater. Eng. 5 (1) (2011) 14–24.
[6] W. Li, N.A. Noda, H. Sakai, Y. Takase, Thermal stress analysis for shrink fitting system used for ceramics conveying rollers in the process of separation, Key Eng. Mater. 452–453 (2011) 241–244.
[7] S. Dedi, N.A. Noda, Y. Sano, Y. Takase, S. Dedi, N.A. Noda, Y. Sano, Y. Takase, Ceramics/steel joint selection for the ceramics roller used at high temperature, Proceeding of the 4th ACEE 2014, pp. 221–222.
[8] S. Harada, N.A. Noda, O. Uehara, M. Nagano, Tensile strength of hot isostatic pressed silicon nitride and effect of specimen dimension, Trans. JSME Ser. A 57 (539) (1991) 1637–1642 (in Japanese).
[9] E. Ogawa, K. Shimizu, S. Hamayoshi, Practical evaluation of large ceramic rolls for continuous hot dipping steel sheet production line, Hitachi Met. Tech. Rev. 28 (2012) 50–55 (in Japanese).
[10] N.A. Noda, M. Yamada, Y. Sano, S. Sugiyama, S. Kobayashi, Thermal stress for all-ceramics rolls used in molten to produce stable high quality galvanized steel sheets, Eng. Fail. Anal. 15 (4) (2008) 261–274.
[11] E. Ogawa, et al., Development of 100% ceramic pot rolls for continuous hot dip coating lines of the steel sheet, Proceedings of 8th International Conference on Zinc and Zinc Alloy Coated Steel Sheet, 6 2011, pp. 1–8.

[12] N.A. Noda, Hendra, M. Oosato, K. Suzumoto, Y. Takase, W. Li, Strength analysis for shrink fitting system used for ceramics rolls in the continuous pickling line, Key Eng. Mater. 462–463 (2011) 1140–1145.
[13] S. Matsuda, D. Suryadi, N.A. Noda, Y. Sano, Y. Takase, S. Harada, Structural design for ceramics rollers used in the heating furnace, Trans. JSME Ser. A 79 (803) (2013) 989–999 (in Japanese).
[14] C.E. Truman, J.D. Booker, Analysis of a shrink-fit failure on a gear hub/shaft assembly, Eng. Fail. Anal. 14 (2007) 557–572.
[15] N. Antoni, Contact separation and failure analysis of a rotating thermo-elastoplastic shrink-fit assembly, Appl. Math. Model. 37 (2003) 2352–2363.
[16] A. Rusin, G. Nowak, W. Piecha, Shrink connection modelling of the steam turbine rotor, Eng. Fail. Anal. 34 (2013) 217–227.
[17] Iron and steel institute of Japan, Steel Handbook. , Maruzen co., Ltd., Tokyo, 1962.
[18] S.P. Timoshenko, J.N. Goodier, Theory of Elasticity, McGraw-Hill Kogakusha Ltd., Tokyo, 1970. 81–82.
[19] Marc Mentat team, Theory and User Information. Vol. A, MSC. Software, Tokyo, 2008. 532.